Advances in Geo-Energy Research

Vol. 19, No. 3, p. 216-230, 2026

Original article

# Geological $CO_2$ storage in heterogeneous saline aquifers: Insights into the mechanisms of thermal and density effects

Aohan Jin[1], Eungyu Park[2], Cai Li[3], Wenguang Shi[1], Quanrong Wang[1,4]*

[1]*School of Environmental Studies, China University of Geosciences, Wuhan 430074, P. R. China*

[2]*Department of Geology, Kyungpook National University, Daegu 41566, Republic of Korea*

[3]*Hainan Branch, CNOOC (China) Limited, Haikou 570100, P. R. China*

[4]*MOE Key Laboratory of Groundwater Quality and Health, China University of Geosciences, Wuhan 430078, P. R. China*

**Keywords:**
Geological $CO_2$ storage
thermal-hydraulic-mechanical simulation
thermal effects
density-driven convection
heterogeneous saline aquifers

**Cited as:**
Jin, A., Park, E., Li, C., Shi, W., Wang, Q. Geological $CO_2$ storage in heterogeneous saline aquifers: Insights into the mechanisms of thermal and density effects. Advances in Geo-Energy Research, 2026, 19(3): 216-230.
https://doi.org/10.46690/ager.2026.03.02

**Abstract:**
Variations in brine density are crucial for both $CO_2$ plume migration and long-term geological $CO_2$ storage. These variations are primarily controlled by three factors: Pressure buildup, $CO_2$ dissolution, and thermal effects. However, previous models have generally neglected these processes or focused mainly on density variations induced by $CO_2$ dissolution. This study establishes a comprehensive thermo-hydro-mechanical framework to capture $CO_2$ migration dynamics in heterogeneous saline aquifers, accounting for brine density variations driven by multiple factors. Eight heterogeneous scenarios, including both high- and low-permeability reservoirs, are constructed to represent the realistic subsurface conditions. Results indicate that thermal effects generate a localized cold front in the near-wellbore region, where $CO_2$ thermodynamic properties are highly temperature-sensitive and differ by several-fold from those of the undisturbed reservoir. Additionally, thermal effects lead to a noticeable decrease in brine density and induce thermal deformation. Brine-density variation is governed primarily by pressure build-up and $CO_2$ dissolution. The incorporation of $CO_2$ dissolution in the thermo-hydro-mechanical model shortens the $CO_2$ plume length by more than 230 m. Pressure build-up is the primary driver for brine density increases in low-permeability reservoirs, whereas $CO_2$ dissolution plays a more significant role in high-permeability reservoirs. Furthermore, high-permeability reservoirs are more conducive to density-driven convection, where vigorous convective fingering enhances mixing and promotes solubility trapping.

## 1. Introduction

Over the past 50 years, the increase in average global temperature has been primarily attributed to elevated atmospheric concentrations of human-induced greenhouse gases, including methane ($CH_4$), carbon dioxide ($CO_2$) and so on (Al Baroudi et al., 2021; Ali et al., 2022; Jin et al., 2025). As one of the most efficient strategies for mitigating climate change and realizing carbon neutrality, geological $CO_2$ storage (GCS) has attracted increasing attention and holds great potential for future development (Krevor et al., 2023; Wei et al., 2025). Among various GCS alternatives, deep saline formations are prioritized as the premier choice owing to their vast sequestration volume and widespread availability, making them the preferred storage candidates for large-scale GCS projects (Al Baroudi et al., 2021; Ali et al., 2022). However, formidable challenges remain in improving the long-term security and efficiency of GCS projects due to complex subsurface processes involving multiple physical couplings in heterogeneous reservoirs.

Yandy Scientific Press

*Corresponding author.
*E-mail address*: ahjin@cug.edu.cn (A. Jin); egpark@knu.ac.kr (E. Park); licai1@cnooc.com.cn (C. Li); swg@cug.edu.cn (W. Shi); wangqr@cug.edu.cn (Q. Wang).

Received December 5, 2025; revised January 11, 2026; accepted February 5, 2026; available online February 9, 2026.

Although extensive research has examined various aspects of GCS simulations, including thermal-hydraulic (TH) and hydro-mechanical (HM) coupling (Liu et al., 2020, 2024), a thorough understanding of the complex thermo-hydro-mechanical (THM) behavior inherent in multiphase $CO_2$-water systems remains limited. Many existing models simplify the problem by focusing on single-phase fluids or by neglecting critical THM interactions, which undermines the capacity to capture the long-term performance and reliability of GCS operations (Gan et al., 2021; Mahmoodpour et al., 2022). The injection of cold fluid into hot reservoir rocks further exacerbates thermoelastic stress, and the thermodynamic properties of $CO_2$ exhibit strong temperature dependence. Such a substantial thermal discrepancy between the injected $CO_2$ and the ambient reservoir environment further complicates the non-isothermal coupling effects within the reservoir (Gao et al., 2023, 2025). Furthermore, the inherent heterogeneity of deep sedimentary reservoirs, arising from lithological diversity, fractures, facies variation, and faulting, leads to spatially variable porosity and permeability fields (Aminu et al., 2017; Ershadnia et al., 2020). Formation-scale heterogeneity has been demonstrated to significantly influence $CO_2$ plume morphology and migration patterns, thereby affecting the effective carbon storage capacity (Han et al., 2012; Gao et al., 2023). Furthermore, $CO_2$ plume evolution is strongly influenced by micro-scale geological heterogeneities, including sedimentary laminae, stratification, and argillaceous interbeds (Abidoye et al., 2015; Lyu et al., 2025). Accounting for coupled THM processes in multiphase $CO_2$-water systems and inherent reservoir heterogeneity is essential in GCS projects, as these factors introduce substantial uncertainties into multiphase flow modeling, posing significant challenges to achieving reliable and efficient $CO_2$ storage. Laboratory-scale investigations on diverse sandstone and lithofacies have shown that reservoir heterogeneity not only enhances residual $CO_2$ trapping (Reynolds et al., 2018), but also serves as the primary source of uncertainty in plume behavior (Kou et al., 2021). Recent literature further highlights that the storage potential in fractured reservoirs can be substantially enhanced through matrix-fracture interactions, with improvements of up to 2.8 times (Sohal et al., 2021, 2025). While the impact of geological heterogeneity on $CO_2$ migration and trapping efficiency is well-documented, these studies have not adequately account for the evolution of porosity and permeability caused by volumetric, compressive, and thermal deformation of the solid skeleton, thereby limiting their practical applicability.

Moreover, the dissolution of supercritical $CO_2$ into the aqueous phase can increase brine density by 0.1%-1%, thereby initiating gravitational instabilities (Lu et al., 2009; Meng and Jiang, 2014). Diersch and Kolditz (2002) pointed out that variations in brine density during $CO_2$ injection can be induced by three factors: Pressure build-up, $CO_2$ dissolution, and thermal expansion. The Rayleigh number is commonly employed as a threshold for the onset of density-driven convection, which is initiated when its value exceeds $4\pi^2$ (Otero et al., 2004). Unlike slow molecular diffusion, density-driven convection enhances fluid mixing and promotes $CO_2$ dissolution, thereby significantly contributing to storage efficiency and long-term storage security (Pau et al., 2010, 2014, 2019). Laboratory investigations have shown that even slight variations in boundary conditions, such as aquifer slope, can significantly enhance buoyancy-driven convective flow relative to horizontal settings (MacMinn and Juanes, 2013). Additional field-scale evidence at Bravo Dome was provided by Sathaye et al. (2014), revealing that the observed dissolved $CO_2$ exceeded predictions based solely on molecular diffusion, thus demonstrating the contribution of a density-driven convective mechanism. Beyond stratigraphic geometry, the presence of preferential flow paths, such as reservoir heterogeneity and fractures, introduces additional complexity. Recent studies have demonstrated that reservoirs with high-angle fractures and reversed rhythms tend to enhance $CO_2$ solubility trapping (Kim et al., 2019; Xu et al., 2024; Zhang et al., 2024). Nevertheless, these models adopted a simplified single-phase framework ($CO_2$-rich and $CO_2$-free brines), neglecting crucial physical mechanisms, such as $CO_2$ dissolution and capillary pressure effects. These simplifications tend to overestimate the onset of convective instabilities and to underestimate the corresponding flux of dissolved $CO_2$ (Martinez and Hesse, 2016; Lyu et al., 2023).

To overcome the above limitations, this study proposes an integrated THM model for geological $CO_2$ storage that accounts for porosity and permeability evolution driven by compressive and thermal deformation of the solid skeleton, as well as brine density variations induced by pressure build-up, $CO_2$ dissolution, and thermal expansion. Eight heterogeneous scenarios, including both high- and low-permeability reservoirs, are constructed to represent the realistic subsurface conditions. The pressure- and temperature-dependent thermodynamic properties (density, viscosity, thermal conductivity, and specific heat capacity) are characterized using the REFPROP dataset. This study provides deeper insights into the coupling between THM processes and brine density variations in GCS projects under complex subsurface conditions.

## 2. Model setup

### 2.1 Governing equations

In this study, a two-dimensional rectangular domain is employed to simulate the coupled two-phase THM processes involved in GCS. The heterogeneous saline aquifer is situated at a depth of 1,000 m and spans 5,000 m in length and 100 m in thickness. A geothermal gradient of 25 K/km is adopted, together with a surface temperature of 288.15 K, to define the subsurface thermal environment. The *in-situ* reservoir conditions at this depth exceed the critical point of $CO_2$, which is favorable for long-term GCS. The initial pore pressure field is hydrostatic. Furthermore, the undisturbed *in-situ* stress field satisfies the following conditions: The vertical stress ($\sigma_v = \int \rho_m g \mathrm{d}z$) corresponds to lithostatic pressure caused by gravitational loading, while the horizontal stress ($\sigma_h$) is assumed to be proportional to the vertical stress ($\sigma_h = 0.7\sigma_v$). After being injected into the saline aquifer, $CO_2$ migrates upward by overcoming capillary pressure and accumulates beneath the caprock, thereby establishing a localized $CO_2$-rich zone. A schematic of the conceptual model is presented in Fig. 1.

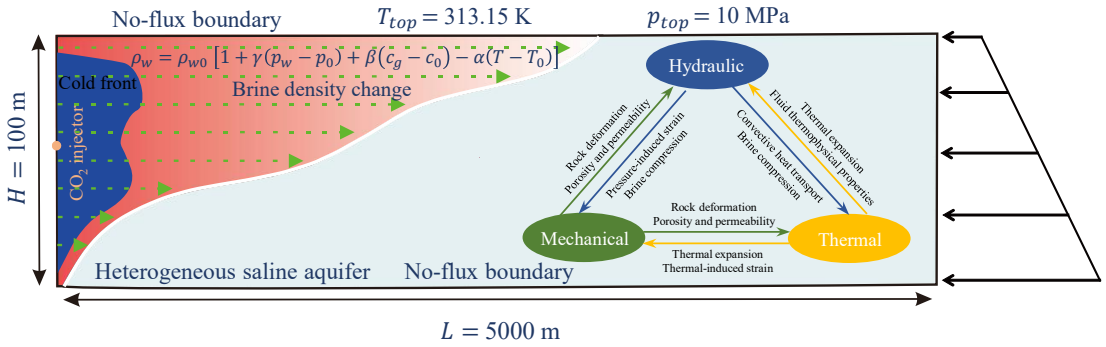


**Fig. 1**. Schematic diagram of multiphase $CO_2$-water flow in a heterogeneous reservoir.

### 2.1.1 Fluid flow equations

The injection of pure $CO_2$ into the subsurface saline reservoirs leads to a complex two-phase flow regime, consisting of a $CO_2$-rich phase and a $CO_2$-free brine phase. Under typical reservoir conditions, the solubility of $CO_2$ in the aqueous phase is approximately 5% by mass (Nordbotten et al., 2005; Wei et al., 2025), and the system involves intricate multiphase and multicomponent interactions. Assuming that $CO_2$ dissolution within the aqueous phase is mass transfer governed, the interphase mass exchange can be quantitatively characterized using a kinetic model (Martinez and Hesse, 2016):

$$\frac{\partial(\rho_g s_g \phi)}{\partial t} + \nabla\cdot(\rho_g u_g) = Q_g - Q_{lg} \tag{1}$$

$$\frac{\partial(\rho_w s_w \phi)}{\partial t} + \nabla\cdot(\rho_w u_w) = Q_w + Q_{lg} \tag{2}$$

where Eqs. (1) and (2) represent the mass conservation equations of the $CO_2$ and brine phases, respectively; $\rho_g$ and $\rho_w$ are the densities of the $CO_2$ and brine phases, respectively (kg/m$^3$); $s_g$ and $s_w$ are the saturation of the $CO_2$ and brine phases, respectively (-); $\phi$ is the porosity of the porous matrix (-); $t$ is the time (s); $Q_g$ and $Q_w$ are the source/sink terms of the $CO_2$ and brine phases, respectively (kg/m$^3$/s); $Q_{lg}$ is the mass of dissolved $CO_2$ in brine per unit volume and time (kg/m$^3$/s); $u_g$ and $u_w$ are the velocities of the $CO_2$ and brine phases, respectively (m/s), and can be calculated using Darcy's law (Vilarrasa et al., 2014; Pavan et al., 2024):

$$u_i = -\frac{k_{ri}k}{\mu_i}(\nabla p_i - \rho_i g) \tag{3}$$

where $k$ is the absolute permeability tensor of the porous medium (m$^2$); $k_{ri}$ is the relative permeability of each phase; $\mu_i$ is the dynamic viscosity of each phase (Pa·s); $p_i$ is the fluid pressure of each phase (Pa); $g$ is the gravity acceleration (m/s$^2$); $i = 1$ and 2 denote the $CO_2$ and brine phases, respectively.

Furthermore, this study considers the impacts of rock skeleton deformation and temperature variations on the pore pressure field. The corresponding continuity equation is derived based on the principles of thermal pore elasticity theory (Li et al., 2016; Wei et al., 2025). Detailed information is provided in Appendix A of the Supplementary file.

$$Q_g = -\rho_g b\frac{\partial \varepsilon_{vol}}{\partial t} + 3\rho_g \alpha_T \frac{\partial T}{\partial t} + q_g \tag{4}$$

$$Q_w = -\rho_w b\frac{\partial \varepsilon_{vol}}{\partial t} + 3\rho_w \alpha_T \frac{\partial T}{\partial t} + q_w \tag{5}$$

where the first term $\rho_w b(\partial\varepsilon_{vol}/\partial t)$ describes the mechanical coupling (kg/m$^3$/s), the second term $\rho_g\alpha_T(\partial T/\partial t)$ represents the thermal coupling (kg/m$^3$/s), and $q_g$ and $q_w$ are the external source/sink terms of the $CO_2$ and brine phases (kg/m$^3$/s), respectively; $b = 1 - K/K_s$ is the Boit coefficient (-); $K$ and $K_s$ are the moduli of the rock mass and solid skeleton (Pa), respectively; $\varepsilon_{vol}$ is the volumetric strain (-); $T$ is the temperature (K); $\alpha_T$ is the linear thermal expansion coefficient of the rock mass (K$^{-1}$), which is defined as $\alpha_T = (1-\phi)\alpha_s + \phi\alpha_f$; $\alpha_s$ and $\alpha_f$ are the linear thermal expansion coefficients of the solid skeleton and fluid (K$^{-1}$), respectively. Additionally, some auxiliary equations are also needed to constrain the quantities:

$$s_g + s_w = 1 \tag{6}$$

$$p_c = p_g - p_w \tag{7}$$

where $p_c$ is the capillary pressure between the $CO_2$ and brine phases (Pa). In this study, the van Genuchten model (van Genuchten, 1980) is employed to determine the capillary pressure and relative permeabilities of the $CO_2$ and brine phases:

$$\bar{s}_w = \frac{s_w - s_{rw}}{1 - s_{rw} - s_{rg}} \tag{8}$$

$$k_{rw} = (\bar{s}_w)^l\left[1 - \left(1 - \bar{s}_w^{1/m}\right)^m\right]^2 \tag{9}$$

$$k_{rg} = (1-\bar{s}_w)^l\left(1 - \bar{s}_w^{1/m}\right)^{2m} \tag{10}$$

where $\bar{s}_w$ is the effective saturation of the brine phase (-); $s_{rw}$ and $s_{rg}$ are the residual saturation of the brine and $CO_2$ phases (-), respectively; $k_{rw}$ and $k_{rg}$ are the relative permeabilities of the brine and $CO_2$ phase, respectively; $m$ and $l$ are constitutive constants in the van Genuchten model.

The solubility of $CO_2$ in brine is affected by the pre-existing concentration of dissolved $CO_2$. Accordingly, evaluating the spatial distribution of dissolved $CO_2$ requires solving an additional solute transport equation (Martinez and Hesse, 2016; Chen et al., 2024):

$$\frac{\partial(c_g\phi s_w)}{\partial t} + \nabla\cdot(c_g u_w) - \nabla\cdot(\phi s_w D\nabla c_g) = S \tag{11}$$

$$S = k_d[\min(\phi s_w c_{sg}, \phi s_g c_{0g}) - c_g] \tag{12}$$

where $c_g$ is the concentration of dissolved $CO_2$ (mol/m$^3$); $D$ is the effective diffusion coefficient (m$^2$/s); $S = Q_g/M_g$ is the

concentration of dissolved $CO_2$ per unit time (mol/m$^3$/s); $M_g$ is the molar mass of $CO_2$ (kg/mol); $k_d$ is the $CO_2$ mass transfer rate between the brine and $CO_2$ phase (s$^{-1}$); $c_{sg}$ is the saturation concentration of dissolved $CO_2$ in brine (mol/m$^3$); $c_{0g}$ is the pure $CO_2$ concentration (mol/m$^3$). Eq. (12) ensures that the concentration of dissolved $CO_2$ never exceeds the available $CO_2$ in the non-wetting phase and the maximum equilibrium concentration prescribed by *in-situ* reservoir conditions.

Moreover, the brine density variations induced by brine compression, $CO_2$ dissolution, and thermal expansion can be represented by a state equation that couples the above equations (Diersch and Kolditz, 2002; Xu et al., 2024):

$$\rho_w = \rho_{w0}\left[1+\gamma(p_w-p_0)+\beta(c_g-c_0)-\alpha(T-T_0)\right] \quad (13)$$

where $\rho_{w0}$ is the density of the $CO_2$-free brine (kg/m$^3$); $p_0$ is the initial reservoir pressure (Pa); $c_0$ is the initial concentration of dissolved $CO_2$ (mol/m$^3$); $T_0$ is the initial reservoir temperature (K); $\gamma$ is the compressibility of the brine (Pa$^{-1}$); $\beta$ is the solute expansion coefficient (m$^3$/mol); $\alpha$ is the thermal expansion coefficient (K$^{-1}$).

### 2.1.2 Momentum balance equations

The porous medium is idealized as a set of overlapping continua, comprising a solid-skeleton phase and a fluid phase. Under the quasi-static assumption, the momentum conservation equation of the system can be written as (Li et al., 2016; Wei et al., 2025):

$$\nabla\cdot\sigma+\rho_m g=0 \quad (14)$$

where $\sigma$ is the total stress tensor (Pa); $\rho_m=\phi\sum\rho_i s_i+(1-\phi)\rho_r$ is the saturated density of the rock mass (kg/m$^3$); $\rho_r$ is the rock density (kg/m$^3$).

According to the principle of effective stress, the bulk stress imposed on the geological formation is partitioned between the solid matrix and the pore fluid, with the Biot coefficient quantifying the fluid's contribution to the total stress load (Kasani and Selvadurai, 2023; Wei et al., 2025). Accordingly, the total stress can be written as follows:

$$\sigma = C:\left(\varepsilon-\varepsilon_{th}-\varepsilon_{pl}\right)-bpI \quad (15)$$

$$\varepsilon=\frac{\nabla s+(\nabla s)^T}{2} \quad (16)$$

$$\varepsilon_{th}=\alpha_T(T-T_0)I \quad (17)$$

where $C$ is the stiffness matrix (Pa); $\varepsilon$ is the total strain (-); $\varepsilon_{th}$ denotes the thermal strain tensor (-); $\varepsilon_{pl}$ is the plastic strain (-); $s$ is the displacement vector (m); $I$ is the identity matrix; $p=\sum p_i s_i$ is the total average pore pressure (Pa). The inclusion of the thermal strain tensor $\varepsilon_{th}$ in Eq. (15) accounts for the thermo-mechanical coupling, i.e., the temperature decrease near the injection well induces contraction of the rock matrix, which redistributes the stress field and may increase the physical properties of reservoir.

### 2.1.3 Heat transfer equations

Assuming local thermal equilibrium between the rock and fluids, the heat transfer process can be described by accounting for thermal conduction and convection (Wu et al., 2023; Pavan et al., 2024):

$$(\rho C_p)_e\frac{\partial^T T}{\partial t}+(\rho_w C_{pw}u_w+\rho_g C_{pg}u_g)\cdot\nabla T-\nabla\cdot(\lambda_e\nabla T)=Q_T \quad (18)$$

$$(\rho C_p)_e=\phi(\rho_w C_{pw}s_w+\rho_g C_{pg}s_g)+(1-\phi)\rho_r C_{pr} \quad (19)$$

$$\lambda_e=\phi(\lambda_w s_w+\lambda_g s_g)+(1-\phi)\lambda_r \quad (20)$$

where $(\rho C_p)_e$ is the effective heat capacity (J/(m$^3$·K)); $C_{pw}$, $C_{pg}$ and $C_{pr}$ are the specific heat capacities of water, $CO_2$, and rock (J/(kg·K)), respectively; $Q_T$ is the volume heat source (W/m$^3$); $\lambda_e$ is the effective thermal conductivity of the reservoir (W/(m·K)); $\lambda_w$, $\lambda_g$ and $\lambda_r$ are the thermal conductivities of water, $CO_2$, and rock (W/(m·K)), respectively. The energy balance equations account for both thermal conduction in the rock-fluid system and thermal convection associated with the migrating $CO_2$ plume. This enables the model to accurately track the movement of the cold front, which is essential for evaluating the temperature-dependent thermodynamic properties of $CO_2$.

Given the temperature difference between the injected $CO_2$ and the reservoir, it is assumed that a heat source is located at the injection well:

$$Q_h=C_{pg}M_{inj}(T_{inj}-T) \quad (21)$$

where $M_{inj}$ is the mass flux of $CO_2$ (kg/m/s), $T_{inj}$ is the temperature of injected $CO_2$ (K).

As supercritical $CO_2$ simultaneously exhibits both the high density of liquids and low viscosity of gases, its thermodynamic properties (density, viscosity, thermal conductivity, and specific heat capacity) are highly sensitive to *in-situ* pressure and temperature conditions (Qu et al., 2017; Gudala et al., 2023). The REFPROP dataset, published by the National Institute of Standards and Technology (NIST), is widely recognized as the authoritative source for accurate thermodynamic data of $CO_2$ (Zhou et al., 2020; Wei et al., 2025). In this study, the REFPROP dataset is integrated into COMSOL Multiphysics® to develop interpolated thermodynamic property functions spanning a temperature range of 280-450 K and a pressure range from 10 to 80 MPa. The thermodynamic property variations of $CO_2$ under varying temperature and pressure are presented in Fig. 2.

### 2.1.4 Equations of porosity and permeability evolution

The continuous injection of $CO_2$ leads to alterations in fluid pressure and reservoir temperature, thereby inducing both compressive and thermal deformation of the solid skeleton. The corresponding porosity evolution can be described by Eq. (22). A detailed derivation process is provided in Appendix B of the Supplementary file.

$$\phi=1-(1-\phi_0)\exp\left[-\frac{1}{K_s}(p-p_0)+\alpha_T(T-T_0)-(\varepsilon_{vol}-\varepsilon_{vol\_0})\right] \quad (22)$$

where $\varepsilon_{vol\_0}$ denotes the initial volumetric strain (-).

The corresponding permeability can be calculated using the Kozeny-Carman equation (Li et al., 2016; Soboleva, 2018):

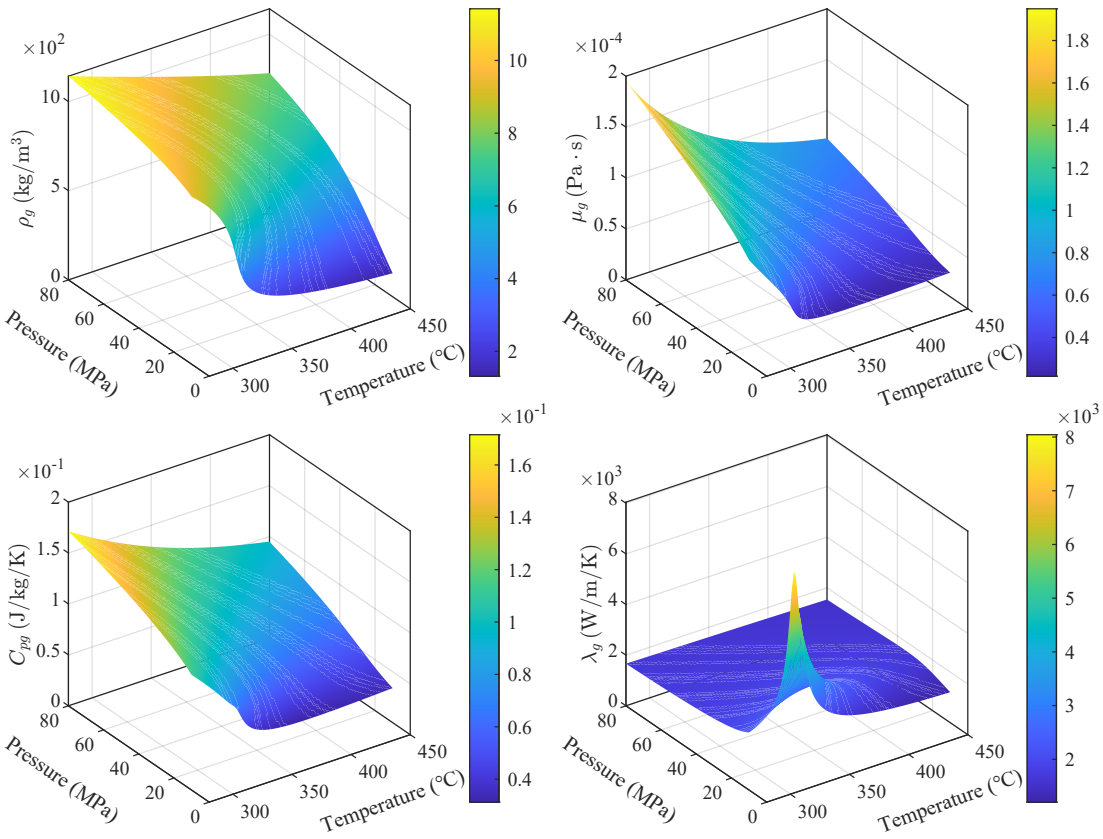


**Fig. 2**. Variation of $CO_2$ thermodynamic properties with temperature and pressure (Temperature range: 280 to 450 K; pressure range: 10 to 80 MPa.

$$k(\phi) = k_0 \left(\frac{\phi}{\phi_0}\right)^3 \left(\frac{1-\phi_0}{1-\phi}\right)^2 \tag{23}$$

where $k_0$ and $\phi_0$ are the original permeability (m$^2$) and porosity (-) of the reservoir, respectively. Collectively, Eqs. (22) and (23) provide the dynamic feedback of the system, translating the complex THM behavior into spatiotemporally variable porosity and permeability in the reservoir.

Regarding boundary conditions, the right boundary is defined as an outflow boundary of the seepage field governed by hydrostatic pressure, while the remaining boundaries are impermeable. For the temperature field, the right boundary is prescribed by the geothermal gradient, whereas the remaining boundaries are insulated. For the displacement field, the lithostatic pressure is represented by a vertical stress load imposed on the upper boundary of the domain.

## 2.2 Numerical model verification

In this study, the finite-element based platform COMSOL Multiphysics® 6.3 (COMSOL Inc., Burlington, MA USA) is employed to perform coupled THM simulations that account for brine density variations during geological $CO_2$ storage in heterogeneous reservoirs. Spatial domains are partitioned into refined quadrilateral four-node elements, complemented by a fully implicit backward Euler technique for time discretization. The nonlinear equations are addressed using a Newton solver integrated with an adaptive time-stepping algorithm, ensuring computational efficiency with a 0.1-year step limit and a 10-iteration threshold.

To verify the accuracy of the present THM framework, the one-dimensional non-isothermal consolidation analytical solution from Liu et al. (2018) is employed as the benchmark. The non-isothermal consolidation model characterizes the soil compaction process induced by the coupled effects of mechanical stress and thermal effects. Detailed information about the benchmark and parameters used for verification is presented in Appendix C of the Supplementary file. A comparative assessment of pore water pressure profiles is shown in Fig. 3, which demonstrates that the proposed THM framework closely aligns with the benchmark solution.

## 2.3 Heterogeneous porosity and permeability

The spatial heterogeneity is incorporated by assigning a pre-defined spatial distribution of initial porosity ($\phi_0$) across the model domain, which subsequently governs the initial permeability field ($k_0$), as defined below (Costa, 2006):

$$k_o = \frac{C_c \phi_0^{\tau}}{1-\phi_o} \tag{24}$$

where $C_c$ and $\tau$ are the Kozeny coefficient (m$^2$) and cementation factors (-). Numerous studies have demonstrated that the porosity of sandstone formations generally follows

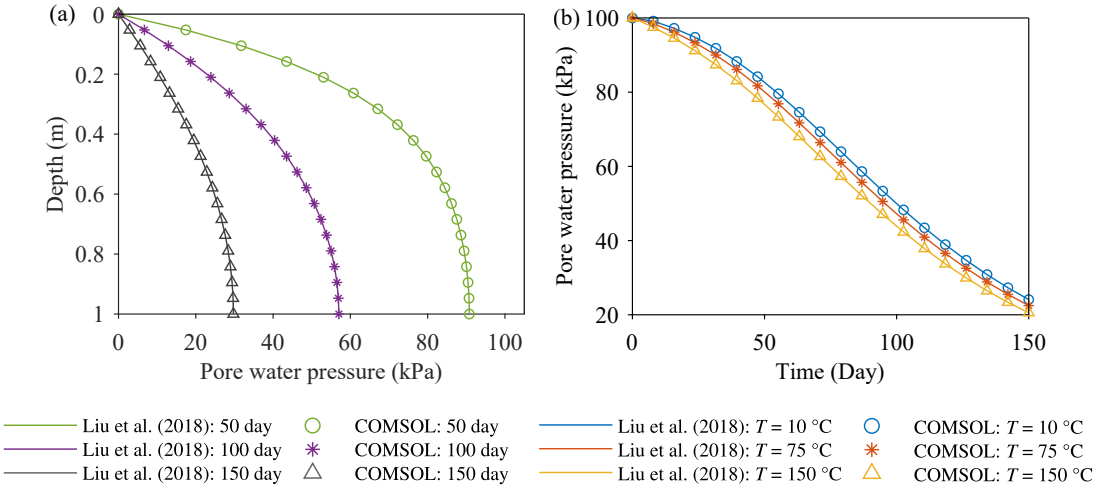


**Fig. 3**. Validation of the numerical model against the analytical solution of Liu et al. (2018): (a) Pore water pressure distribution with depth and (b) pore water pressure variation with temperature.

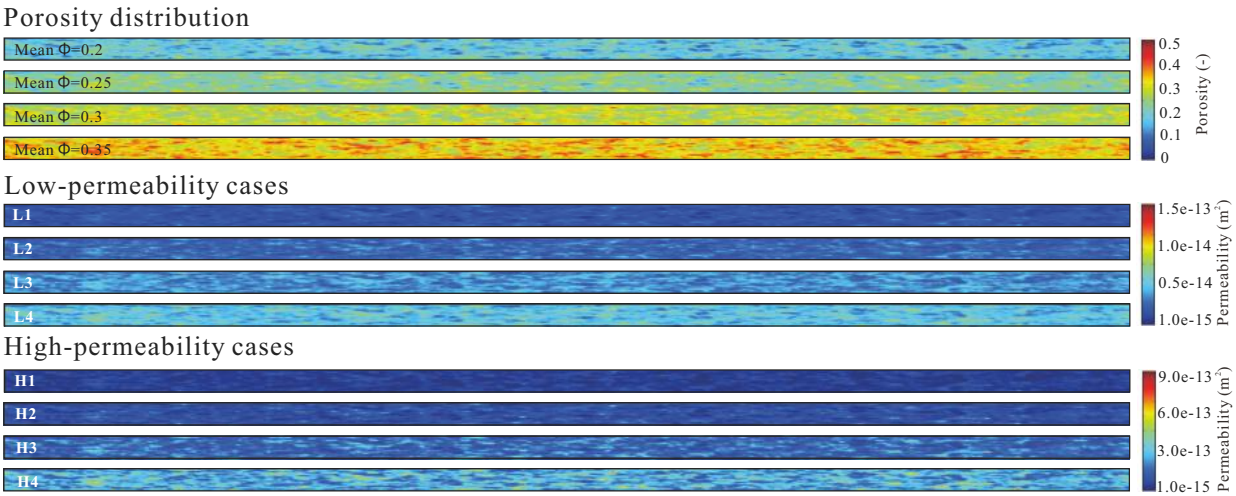


**Fig. 4**. Heterogeneous physical models with different porosity and permeability distributions.

**Table 1**. Different heterogeneity scenarios used in this study.

| Case | Mean $\phi$ (-) | $k$ (mD) | |
|---|---|---|---|
| | | Ranges | Mean |
| L1 | 0.20 | 1.88-61.1 | 18.0 |
| L2 | 0.25 | 2.32-79.4 | 26.4 |
| L3 | 0.30 | 6.16-102 | 36.8 |
| L4 | 0.35 | 13.1-114 | 49.6 |
| H1 | 0.20 | 0.76-352 | 49.3 |
| H2 | 0.25 | 1.12-534 | 92.7 |
| H3 | 0.30 | 6.64-788 | 160 |
| H4 | 0.35 | 20.2-1140 | 259 |

a normal distribution (Falcon-Suarez et al., 2017; Safari et al., 2021; Zech and de Winter, 2023). This study considers four porosity fields, each following a normal distribution with mean values of approximately 0.20, 0.25, 0.30 and 0.35, and a standard deviation of 0.05. Fig. 4 shows the heterogeneous physical models with different porosity and permeability distributions. To characterize the permeability field across different lithologies, such as shale and sandstone, two sets of $C_c$ and $\tau$ values are adopted. Specifically, $C_c = 1.46 \times 10^{-13}$ and $\tau = 1.47$ represent low-permeability reservoirs, while $C_c = 2.8 \times 10^{-12}$ and $\tau = 2.76$ correspond to high-permeability reservoirs (Costa, 2006; Pavan et al., 2024). Table 1 summarizes different heterogeneity cases used in this study. Table 2 summarizes the additional parameters used in the simulations.

## 3. Results and discussion

### 3.1 $CO_2$ migration and reservoir response

The spatial distribution of the $CO_2$ saturation fronts under different heterogeneous reservoirs are illustrated in Fig. 5, highlighting the significant influence of reservoir heterogeneity

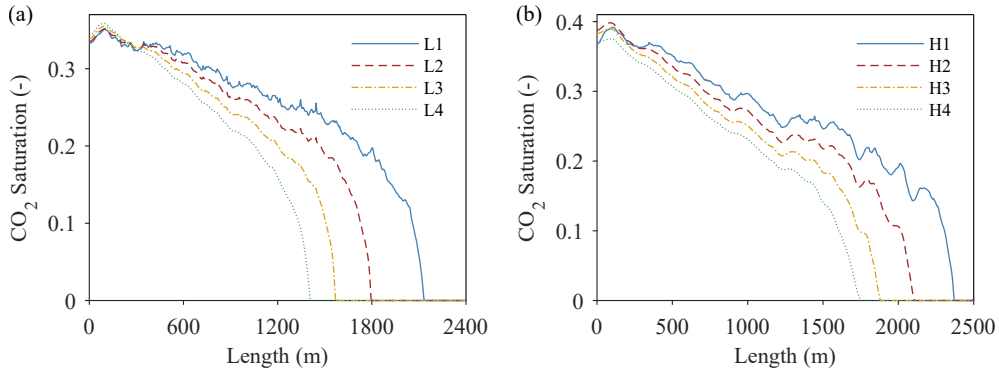


**Fig. 5**. Spatial evolution of $CO_2$ saturation along the reservoir top under different heterogeneous scenarios: (a) Low-permeability reservoirs and (b) high-permeability reservoirs.

**Table 2**. Parameters used in numerical simulations.

| Reference | Parameter | Value | Description |
|---|---|---|---|
| Wei et al. (2025) | $\alpha_T$ ($K^{-1}$) | 2.0e-5 | Thermal expansion coefficient of rock. |
| | $\rho_{w0}$ ($kg/m^3$) | 1,050 | Initial density of brine. |
| | $\rho_{w_max}$ ($kg/m^3$) | 1,100 | Density of brine saturated with $CO_2$. |
| | $\gamma$ ($Pa^{-1}$) | 4.4e-10 | Compressibility of brine. |
| | $m$ (-) | 0.5 | Constitutive constant of the v-G model. |
| | $l$ (-) | 0.5 | Constitutive constant of the v-G model. |
| | $s_{rw}$ (-) | 0.2 | Residual saturation of brine. |
| | $s_{rn}$ (-) | 0 | Residual saturation of $CO_2$. |
| Vilarrasa et al. (2014) | $k_d$ ($s^{-1}$) | 5.0e-8 | Mass transfer rate. |
| Nordbotten et al. (2005) | $\rho_r$ ($kg/m^3$) | 2,600 | Density of solid matrix. |
| | $C_{pr}$ (J/kg/K) | 874 | Specific heat capacity of solid matrix. |
| | $\lambda_r$ (W/m/K) | 1.5 | Thermal conductivity of solid matrix. |
| | $\alpha$ ($K^{-1}$) | 2.5e-4 | Volumetric thermal expansion coefficient. |
| | $\lambda_w$ (W/m/K) | 0.59 | Thermal conductivity of brine. |
| | $C_{pw}$ (J/kg/K) | 4,200 | Specific heat capacity of brine. |
| | $S_{\max}$ (-) | 0.05 | Maximum solubility of $CO_2$ in brine. |
| Cappa and Rutqvist (2011) | $E(d)$ (GPa) | 10 | Elastic modulus. |
| | $\nu$ (-) | 0.25 | Poisson's ratio. |
| | $b$ (-) | 1.0 | Biot coefficient. |
| | $M_{inj}$ (kg/m/s) | 0.02 | Injection rate of $CO_2$. |
| Class et al. (2009) | $p_{ec}$ (kPa) | 200 | Entry capillary pressure. |
| Qu et al. (2012) | $T_{inj}$ (K) | 288.15 | Temperature of injected $CO_2$. |
| Chen et al. (2024) | $\mu_w$ (mPa·s) | 1.0 | Dynamic viscosity of brine. |
| | $D$ ($m^2/s$) | 2.0e-9 | Effective diffusion coefficient. |

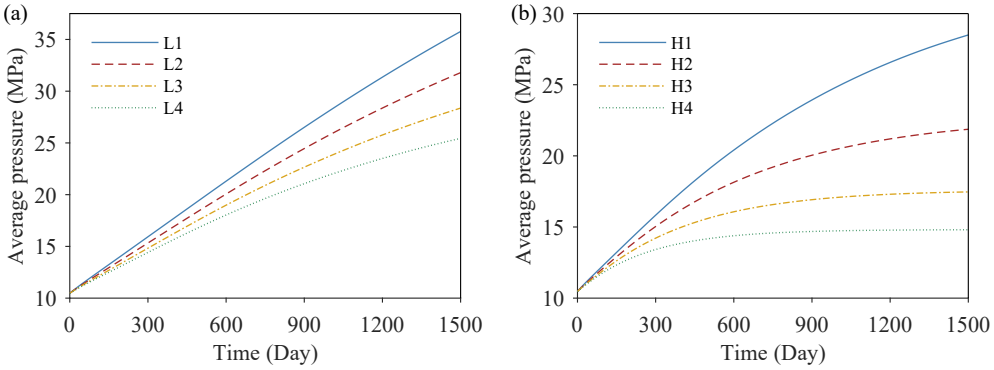


**Fig. 6**. Temporal evolution of average pore pressure under different heterogeneous scenarios: (a) Low-permeability reservoirs and (b) high-permeability reservoirs.

on $CO_2$ migration behavior. As porosity increases from 0.15 to 0.30, the migration distance of $CO_2$ plumes decreases in both low- and high-permeability scenarios since higher porosity enhances the structure trapping capacity of the reservoir. In low-permeability reservoirs, the lateral migration distance of $CO_2$ plumes is limited to 1,409.3-2,133.2 m, while in high-permeability reservoirs, the distance increases to 1,747.7-2,370.3 m. The low-permeability cases also exhibit a smaller $CO_2$ volume fraction and stronger fluctuations at the top of the reservoir compared with high-permeability cases. This can be attributed to the fact that higher porosity generally correlates with a more interconnected pore network, which reduces viscous fingering and lateral extent, while increasing local $CO_2$ saturation. Fig. 6 illustrates the variation in average pore pressure under different heterogeneous conditions, further emphasizing the critical role of reservoir physical properties. The corresponding distribution of pore pressure is presented in Fig. S1 of the Supplementary file. For case L1, low-porosity reservoirs with low permeability impede $CO_2$ migration, resulting in significant pressure build-up exceeding 35.0 MPa after 1,500 days of injection. In contrast, with the increasing porosity, as in Case L4, $CO_2$ migration is enhanced, and pore pressure falls to approximately 25.3 MPa, providing a more favorable pressure regime for long-term storage. Additionally, the high-permeability cases facilitate lateral migration and pressure dissipates, lowering average pressure build-up compared to low-permeability cases.

Furthermore, the dynamic variations in porosity and permeability are influenced by the complex THM coupling mechanisms. To further examine these effects, the relative changes in these parameters are defined as follows:

$$\overline{\Delta\phi}_l = \frac{\int_{\Omega g}\left[\dfrac{\phi_i(x,z)-\phi_0(x,z)}{\phi_0(x,z)}\right]\mathrm{d}x\mathrm{d}z}{\int_{\Omega g}\mathrm{d}x\mathrm{d}z} \tag{25}$$

$$\overline{\Delta k}_l = \frac{\int_{\Omega g}\left[\dfrac{k_i(x,z)-k_0(x,z)}{k_0(x,z)}\right]\mathrm{d}x\mathrm{d}z}{\int_{\Omega g}\mathrm{d}x\mathrm{d}z} \tag{26}$$

where $\overline{\Delta\phi_t}$ and $\overline{\Delta k_t}$ denote the average relative changes in porosity (-) and permeability ($m^2$) due to compressive and thermal deformation of the solid skeleton, respectively; $\phi_i(x,z)$ and $k_i(x,z)$ denote the corresponding spatially change in porosity (-) and permeability ($m^2$); and $\Omega g$ denotes the domain occupied by the $CO_2$ plume. Fig. 7 illustrates the nonlinear evolution of porosity and permeability induced by THM coupling, revealing a markedly amplified permeability response relative to porosity. The corresponding distribution of volumetric strain is presented in Fig. S2 of the Supplementary file. In low-permeability Case L1, permeability ultimately increases by about 9.47%, which is approximately 3.5 times the porosity increase (~2.65%). The results further demonstrate that pressure build-up causes much stronger property changes in low-permeability reservoirs: The maximum permeability increase in Case L1 is nearly 65.8% greater than that in Case H1 and exceeds that in Case L4 by more than three times. This indicates that constrained fluid flow and limited storage capacity lead to pronounced pressure increases and greater poroelastic expansion.

## 3.2 Thermal effects on $CO_2$ migration dynamics

The temperature difference between injected $CO_2$ and the reservoir produces a pronounced cold front around the injection well. Such thermal perturbations alter fluid properties, including $CO_2$ density, viscosity, thermal conductivity, specific heat capacity, and also induce thermal deformation. Fig. 8 shows the temperature field distribution within 300 m of the injection well after 1,500 days, with the cold front exhibiting minimal influence beyond approximately 100 m. This observation is consistent with the conclusions of Vilarrasa et al. (2014), who reported that decades of industrial-scale $CO_2$ injection produced cold regions in reservoir that extend hundreds of meters. Additionally, preferential flow pathways are formed in high-permeability scenarios, as indicated by the white circle in Fig. 8. The corresponding distribution of thermal deformation is shown in Fig. S3 of the Supplementary file, which exhibits consistent patterns with those observed in Fig. 8. The temperature variations along the injection well under different heterogeneous reservoirs are illustrated in Fig. 9. Under low-permeability scenarios, nearly overlapped temperature curves suggest that heat conduction is dominant, and porosity exerts negligible effect on temperature distribution.

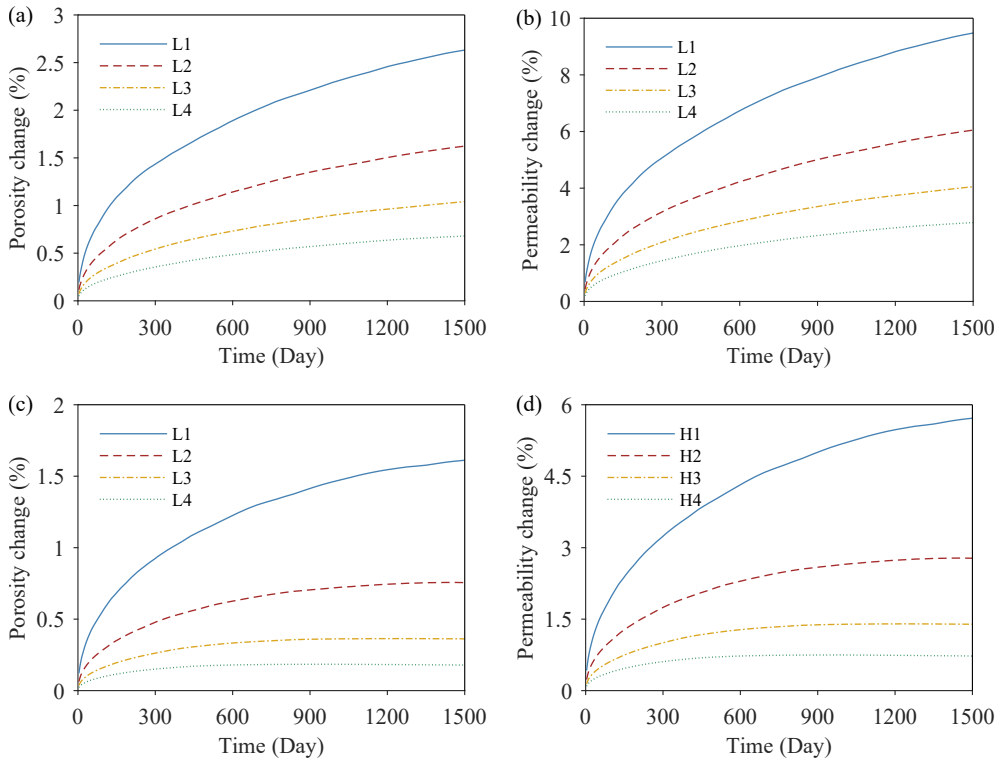


**Fig. 7**. Temporal evolution of porosity and permeability within the domain occupied by $CO_2$ plumes: (a)-(b) Low-permeability reservoirs and (c)-(d) high-permeability reservoirs.

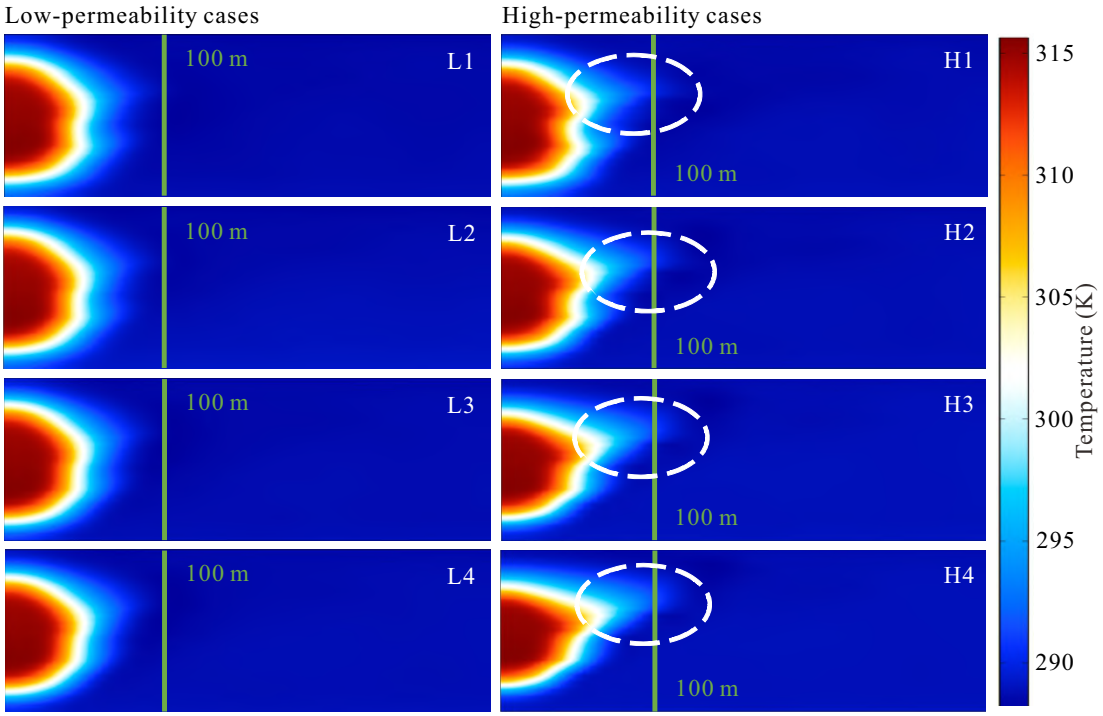


**Fig. 8**. Spatial distribution of temperature field under different heterogeneous conditions.

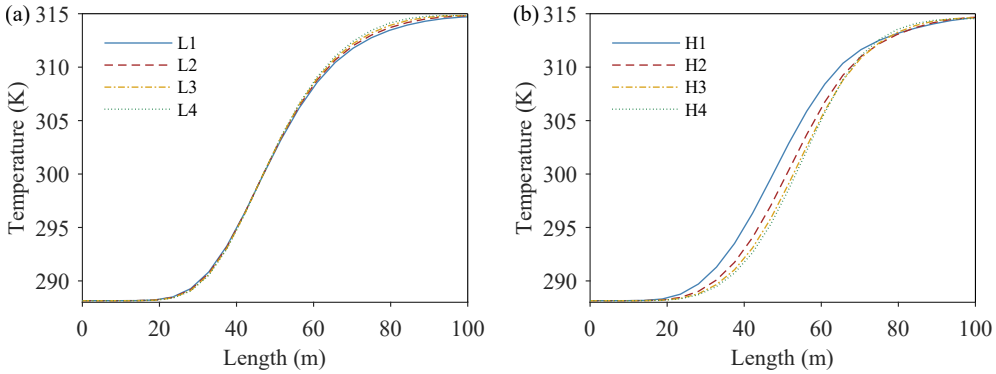


**Fig. 9**. Spatial evolution of temperature along the injection well under different heterogeneous scenarios: (a) Low-permeability reservoirs and (b) high-permeability reservoirs.

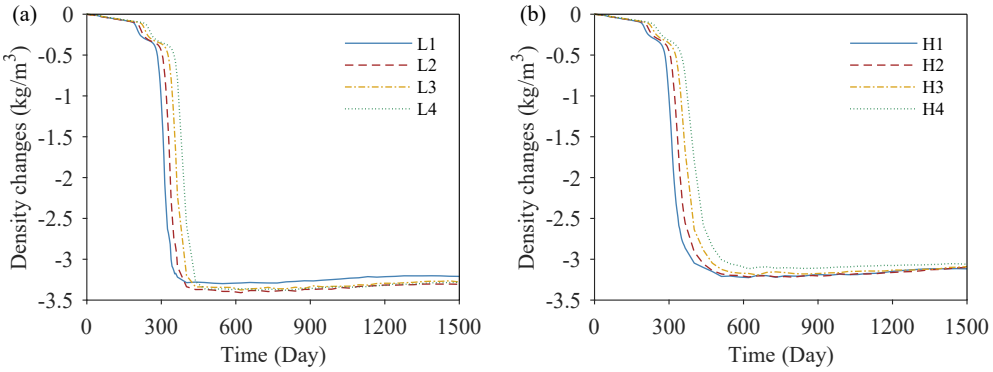


**Fig. 10**. Average density decreases in the cold regions induced by thermal effects under different heterogeneous scenarios: (a) Low-permeability reservoirs and (b) high-permeability reservoirs.

In contrast, in high-permeability scenarios, the curves exhibit significant separation, with Case H4 showing a more rapid advancement of the cold front than Case H1. This behavior can be attributed to a reduction in the effective volumetric heat capacity, which enhances heat-transfer efficiency, thereby leading to a greater thermal breakthrough distance.

The heat exchange between the injected $CO_2$ and the *in-situ* reservoir fluids plays a pivotal role in modulating brine properties through thermal expansion. Fig. 10 illustrates the temporal evolution of brine density induced by temperature difference within the cold front region. The observed dependence of brine density variations on porosity arises from the thermal inertia of the porous medium. In low-porosity Cases (L1 and H1), the reduced effective heat capacity allows the cold front to propagate more rapidly, causing an earlier decrease in brine density. In high-porosity Cases (L4 and H4), the greater brine content per unit volume provides a larger thermal reservoir that moderates temperature changes, leading to a delayed density response. Meanwhile, the ultimate decrease in brine density is approximately -3.5 kg/m$^3$ across all scenarios. This suggests that although hydraulic and structural properties control the transient heat-exchange rate, the final state is a thermally saturated equilibrium governed by the local thermodynamic conditions.

Moreover, the evolution of $CO_2$ thermodynamic properties around the injection well is governed by the interplay between local pressure build-up and thermal equilibration, as illustrated in Fig. 11. The profiles of $CO_2$ density, viscosity, thermal conductivity, and specific heat capacity are consistent with spatial temperature distribution across all scenarios. Notably, even slight temperature fluctuations can cause significant variations in these properties, especially the specific heat capacity. Compared with iso-thermal assumptions, reduced $CO_2$ viscosity enhances storage capacity by promoting faster lateral plume migration, while increased $CO_2$ density mitigates leakage risks by limiting buoyancy-driven upward flow. Meanwhile, higher thermal conductivity and lower specific heat capacity promote the dissipation of thermal anomalies, leading to more rapid thermodynamic equilibrium. These findings underscore the importance of integrated THM models in enhancing the predictive accuracy of long-term $CO_2$ plume dynamics.

## 3.3 Density effects on $CO_2$ migration dynamics

The brine density is affected by three main processes: $CO_2$ dissolution, brine compression and thermal expansion. Considering the absence of a built-in $CO_2$ dissolution module in COMSOL, the dissolution process is represented in this study using a standard mass-transfer formulation. The individual contributions of these mechanisms to brine density variations are quantified as follows:

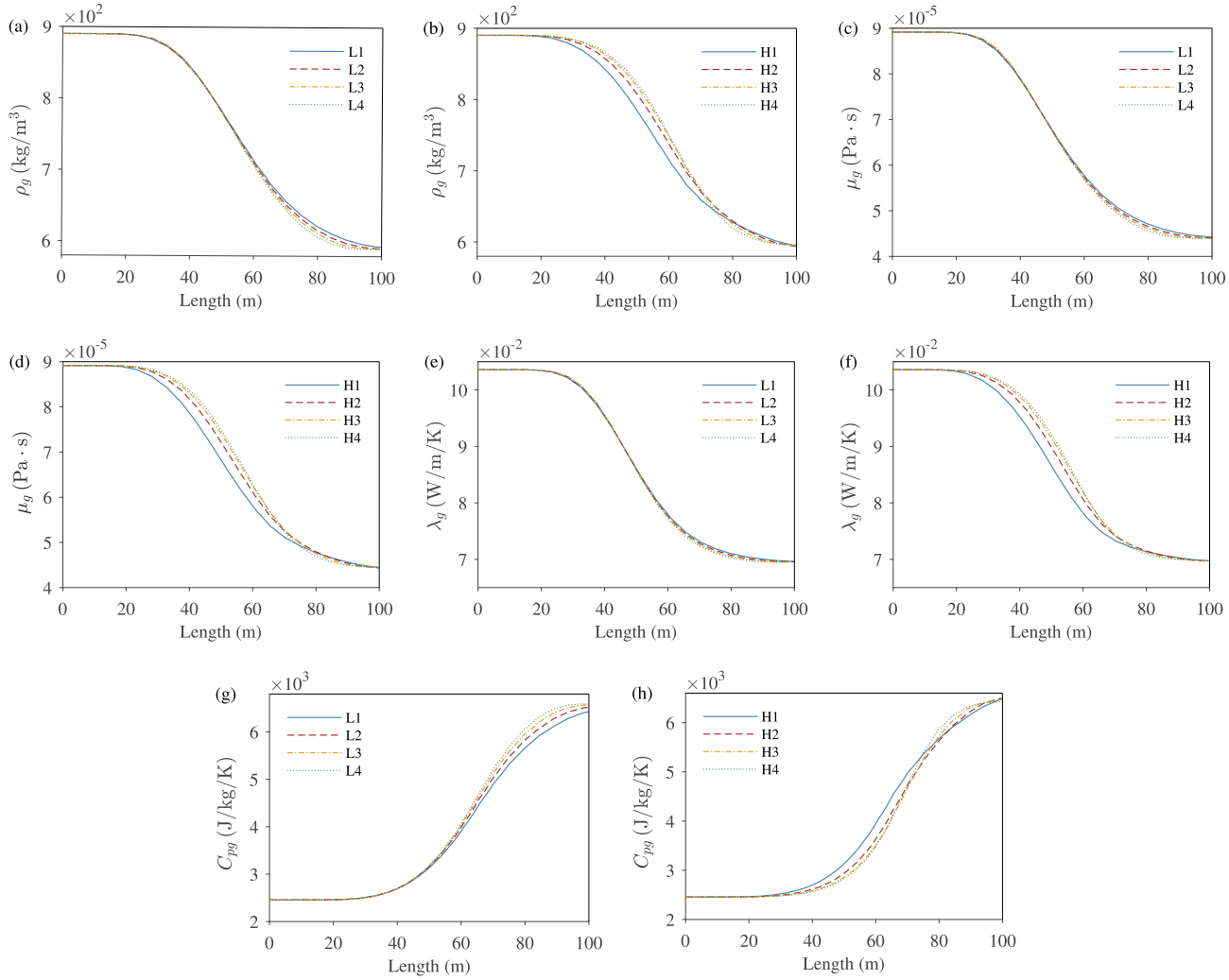


**Fig. 11**. Spatial evolution of $CO_2$ thermodynamic properties along the injection well under different heterogeneous scenarios: (a)-(b) Density, (c)-(d) viscosity, (e)-(f) thermal conductivity and (g)-(h) Specific heat capacity.

$$\overline{\Delta\rho}_l = \frac{\int_{\Omega_g} \rho_i(x,z)\mathrm{d}x\mathrm{d}z}{\int_{\Omega_g} \mathrm{d}x\mathrm{d}z} \tag{27}$$

where $\overline{\Delta\rho_l}$ denotes the average change in brine density (kg/m$^3$) attributed to $CO_2$ dissolution, brine compression and thermal expansion, respectively; $\rho_i(x,z)$ denotes the corresponding spatial change in brine density (kg/m$^3$).

To quantify the relative impact of competing physical and chemical mechanisms on fluid properties, the individual contributions to variations in brine density are analyzed. As presented in Fig. 12, the variations in brine density are predominantly governed by the interplay of brine compression and $CO_2$ dissolution, whereas thermal expansion exerts a negligible influence under the investigated conditions. Specifically, in low-permeability Case L2, substantial pressure accumulation renders brine compression the dominant contributor (approximately 70.5%), while in high-permeability Case H2, $CO_2$ dissolution becomes more significant, contributing approximately 45.6%. Fig. 13 further examines the influence of $CO_2$ dissolution on plume migration and the evolution of average pore pressure. The comparison reveals that dissolution decreases $CO_2$ saturation and reduces plume extent to roughly 239 m in Case L2 and 271 m in Case H2. Meanwhile, it alleviates pore pressure build-up and associated geo-mechanical risks, thereby improving the long-term security of the GCS projects.

Moreover, the overall increase in brine density promotes the development of dissolved $CO_2$ fingers after injection. This density-driven convection enhances fluid mixing and accelerates $CO_2$ dissolution, thereby significantly improving storage efficiency. As shown in Fig. 14, the onset and development of the dissolved $CO_2$ fingers are controlled primarily by permeability. A marked difference can be observed between low-permeability (Cases L1-L4) and high-permeability (Cases H1-H4) scenarios. In high-permeability reservoirs, vigorous convective fingering is fully developed in about 50 years, whereas low-permeability scenarios require nearly 200 years to achieve a comparable plume penetration depth. The temporal evolution of $CO_2$ fingers in both low- and high-permeability reservoirs are presented in Figs. S4 and S5 of the Supple-

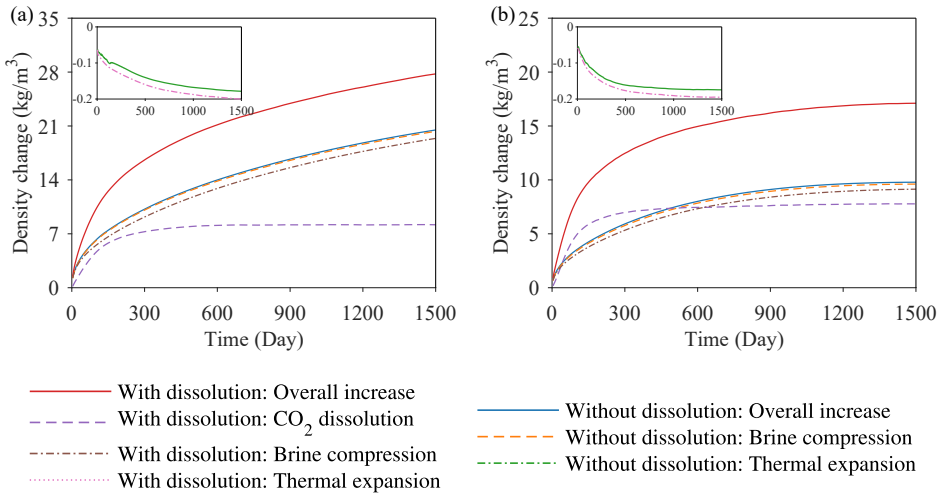


**Fig. 12**. Contributions of $CO_2$ dissolution, brine compression, and thermal expansion to the overall increase in brine density: (a) Case L2 and (b) case H2.

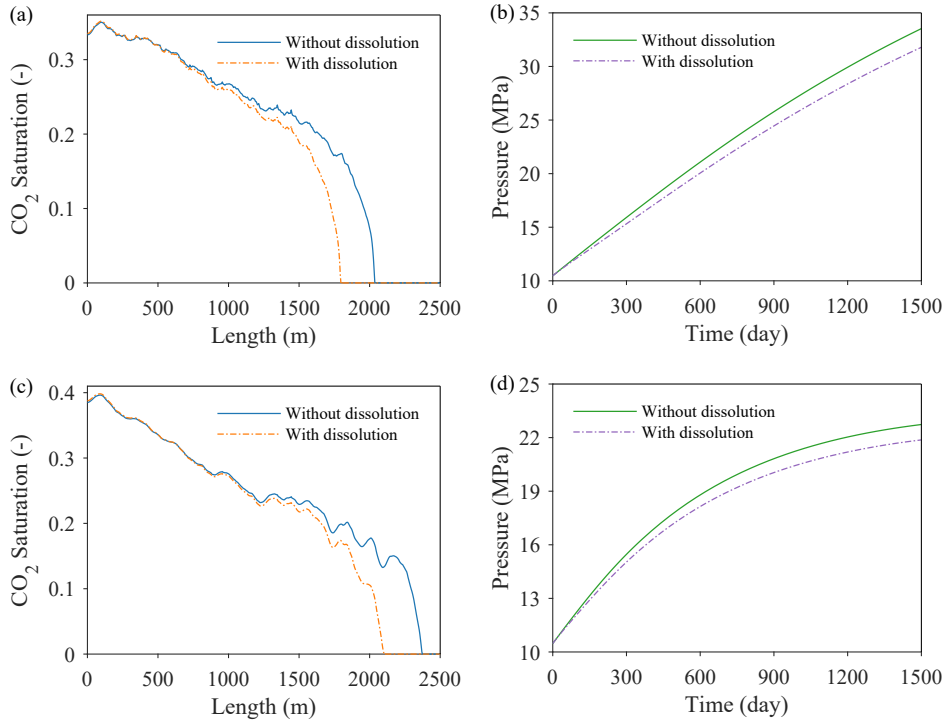


**Fig. 13**. Influence of $CO_2$ dissolution on plume migration and average pore pressure evolution: (a)-(b) Case L2 and (c)-(d) case H2.

mentary file. The diffusion-to-convection transition is driven by gravitational instability in the $CO_2$-saturated brine layer, which is characterized by the critical Rayleigh number (Ra). In high-permeability reservoirs, lower viscous resistance leads to higher Ra, promoting more rapid fingering with complex branching and coalescence. Although both low- and high-permeability scenarios exhibit gravitational instabilities, the rapid development of convective $CO_2$ fingers in the high-permeability scenarios enhances mass transfer across the interface between $CO_2$-saturated brine and $CO_2$-free brine, thereby improving solubility trapping efficiency and the long-term permanence of GCS projects.

## 3.4 Limitations

In the Conclusions, this study proposes an integrated THM framework to simulate $CO_2$ migration dynamics in heterogeneous saline aquifers, accounting for brine density variations driven by pressure build-up, $CO_2$ dissolution, and thermal effects. The findings demonstrate that incorporating density variations within an integrated THM framework is essential

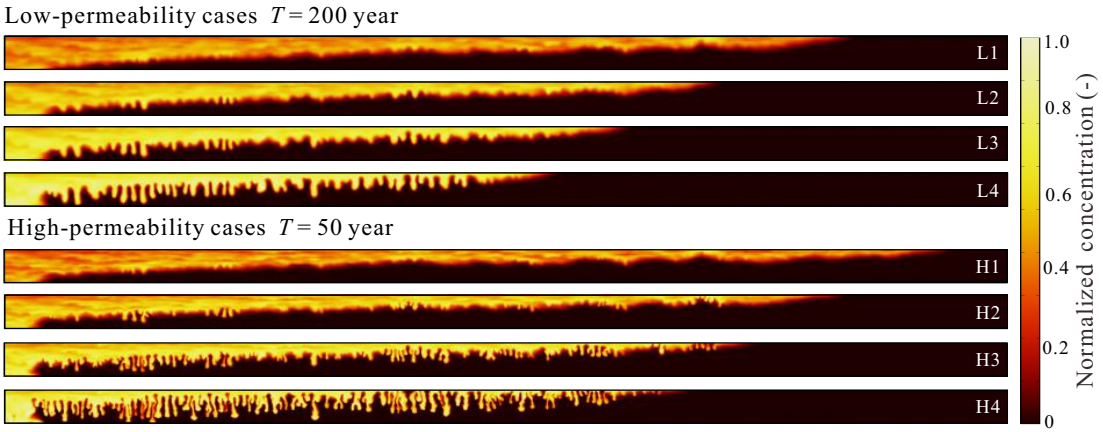


**Fig. 14**. Development of $CO_2$ fingers under different heterogeneous scenarios.

for reliable, long-term forecasts of reservoir behavior, as it captures the intricate coupling among porosity, permeability, temperature, stress, and density dynamics. However, it is imperative to recognize several limitations associated with the present study. Firstly, the $CO_2$ dissolution rate into formation brine is assumed constant. However, the dissolution of $CO_2$ is a kinetically controlled process, that is highly sensitive to *in-situ* environment, including temperature, pressure, and mineralization level. This simplification may overlook spatial and temporal variations in $CO_2$-brine interactions, potentially resulting in inaccurate estimations of solubility trapping efficiency (Martinez and Hesse, 2016; Xu et al., 2024). Secondly, the present model is restricted to a two-dimensional framework, which inherently constrains its capacity to capture the complex three-dimensional flow and migration dynamics of $CO_2$. This simplification may lead to biases in the predicted plume migration, pressure accumulation, and trapping efficiency under realistic field conditions (Singh et al., 2025; Wei et al., 2025). Lastly, the current modeling framework does not incorporate geochemical reactions among injected $CO_2$, formation minerals, and brine. Although these effects are relatively minor relative to the primary hydrodynamic drivers considered in this study, their significance may escalate over centennial timescales or within mineralogically reactive settings, such as carbonate-rich strata (Ali et al., 2022; Moslehi et al., 2025). These limitations highlight the necessity of future modeling efforts toward integrating dissolution kinetics, three-dimensional reservoir structures, and a coupled reactive transport module to enhance predictive reliability and more accurately capture the long-term behavior of GCS projects.

## 4. Conclusions

This study investigates multiphase flow dynamics in heterogeneous saline aquifers during geological $CO_2$ storage, focusing on the spatiotemporal coupling of THM processes and the associated density-driven convection induced by pressure build-up, $CO_2$ dissolution, and thermal expansion. Eight heterogeneous scenarios, including both high- and low-permeability reservoirs, are constructed to represent the realistic subsurface conditions. The analysis reveals the influences of reservoir heterogeneity, thermal effects, and density-driven mechanisms on $CO_2$ migration dynamics. Based on the present analysis, the main conclusions are summarized as follows.

Reservoir porosity and permeability are critical physical properties governing $CO_2$ storage behavior. Higher porosity enhances structural trapping and significantly shortens plume migration, whereas high permeability extends migration distance while lowering pore pressure. Moreover, the evolution of porosity and permeability is controlled by intricate THM interactions, with low-permeability scenarios exhibiting approximately 1.65-3.83 times greater improvements in reservoir properties than the high-permeability reservoirs.

Cold $CO_2$ injection creates a localized thermal front that significantly alters the thermodynamic properties of $CO_2$. High permeability accelerates cold front propagation via preferential flow, whereas in low permeability reservoirs, heat conduction is dominant. Additionally, thermal effects lead to a decrease in brine density of approximately -3.5 kg/m$^3$ and a maximum thermal deformation on the order of $1.2 \times 10^{-4}$. Compared with iso-thermal assumptions, temperature-induced changes in viscosity and density affect both $CO_2$ plume migration and leakage risks, underscoring the importance of coupled THM models.

Brine density variations are controlled primarily by compression in low-permeability reservoirs and by $CO_2$ dissolution in high-permeability scenarios. The incorporation of $CO_2$ dissolution in coupled THM models shortens the $CO_2$ plume by more than 230 m and alleviates pressure build-up, thereby improving long-term storage security. In addition, high permeability facilitates rapid convective fingering and efficient solubility trapping, whereas low-permeability reservoirs remain in the diffusion-dominated regime.

## Acknowledgements

This research was partially supported by the Joint Funds of the National Natural Science Foundation of China (No. U24A20596); the National Natural Science Foundation of China (Nos. 42222704 and 42502228); the Guangxi Science and Technology Major Program (No. AB25069394); the Natural Science Foundation of Hubei Province (No. 2025AFB012),

and the CAST Youth Science and Technology Talent Cultivation Program for Doctoral Students.

## Supplementary file

https://doi.org/10.46690/ager.2026.03.02

## Conflicts of interest

The authors declare no competing interest.



## References

Abidoye, L. K., Khudaida, K. J., Das, D. B. Geological carbon sequestration in the context of two-phase flow in porous media: A review. Critical Reviews in Environmental Science and Technology, 2015, 45(11): 1105-1147.

Al Baroudi, H., Awoyomi, A., Patchigolla, K. et al. A review of large-scale $CO_2$ shipping and marine emissions management for carbon capture, utilisation and storage. Applied Energy, 2021, 287: 116510.

Ali, M., Jha, N. K., Pal, N. et al. Recent advances in carbon dioxide geological storage, experimental procedures, influencing parameters, and future outlook. Earth-Science Reviews, 2022, 225: 103895.

Aminu, M. D., Nabavi, S. A., Rochelle, C. A. et al. A review of developments in carbon dioxide storage. Applied Energy, 2017, 208: 1389-1419.

Cappa, F., Rutqvist, J. Modeling of coupled deformation and permeability evolution during fault reactivation induced by deep underground injection of $CO_2$. International Journal of Greenhouse Gas Control, 2011, 5(2): 336-346.

Chen, R., Xu, W., Chen, Y. A numerical model for evaluating the long-term migration and phase transition behavior of foam-assisted injection of $CO_2$ in saline aquifers. Geoenergy Science and Engineering, 2024, 243: 213328.

Class, H., Ebigbo, A., Helmig, R. et al. A benchmark study on problems related to $CO_2$ storage in geologic formations. Computational Geosciences, 2009, 13(4): 409-434.

Costa, A. Permeability-porosity relationship: A reexamination of the Kozeny-Carman equation based on a fractal pore-space geometry assumption. Geophysical Research Letters, 2006, 33(2): L02318.

Diersch, H. J. G., Kolditz, O. Variable-density flow and transport in porous media: Approaches and challenges. Advances in Water Resources, 2002, 25(8): 899-944.

Ershadnia, R., Wallace, C. D., Soltanian, M. R. $CO_2$ geological sequestration in heterogeneous binary media: Effects of geological and operational conditions. Advances in Geo-Energy Research, 2020, 4(4): 392-405.

Falcon-Suarez, I., Canal-Vila, J., Delgado-Martin, J. et al. Characterisation and multifaceted anisotropy assessment of Corvio sandstone for geological $CO_2$ storage studies. Geophysical Prospecting, 2017, 65(5): 1293-1311.

Gan, Q., Candela, T., Wassing, B. et al. The use of supercritical $CO_2$ in deep geothermal reservoirs as a working fluid: Insights from coupled THMC modeling. International Journal of Rock Mechanics and Mining Sciences, 2021, 147: 104872.

Gao, X., Yang, S., Shen, B. et al. Influence of reservoir spatial heterogeneity on a multicoupling process of $CO_2$ geological storage. Energy & Fuels, 2023, 37(19): 14991-15005.

Gudala, M., Govindarajan, S. K., Yan, B. et al. Comparison of supercritical $CO_2$ with water as geofluid in geothermal reservoirs with numerical investigation using fully coupled thermo-hydro-geomechanical model. Journal of Energy Resources Technology, 2023, 145(6): 061302.

Han, W. S., Kim, K.-Y., Park, E. et al. Modeling of spatiotemporal thermal response to $CO_2$ injection in saline formations: Interpretation for monitoring. Transport in Porous Media, 2012, 93(3): 381-399.

Huppert, H. E., Neufeld, J. A. The fluid mechanics of carbon dioxide sequestration. Annual Review of Fluid Mechanics, 2014, 46: 255-272.

Jin, A., Shi, W., Zhou, R. et al. Inverse modeling of subsurface flow during $CO_2$-enhanced oil recovery using deep learning approach with adaptive learning strategy. Geoenergy Science and Engineering, 2025, 251: 213855.

Kasani, H. A., Selvadurai, A. A review of techniques for measuring the biot coefficient and other effective stress parameters for fluid-saturated rocks. Applied Mechanics Reviews, 2023, 75(2): 020801.

Kim, M., Kim, K.-Y., Han, W. S. et al. Density-driven convection in a fractured porous media: Implications for geological $CO_2$ storage. Water Resources Research, 2019, 55(7): 5852-5870.

Kou, Z., Wang, H., Alvarado, V. et al. Impact of sub-core scale heterogeneity on $CO_2$/brine multiphase flow for geological carbon storage in the upper Minnelusa sandstones. Journal of Hydrology, 2021, 599: 126481.

Krevor, S., de Coninck, H., Gasda, S. E. et al. Subsurface carbon dioxide and hydrogen storage for a sustainable energy future. Nature Reviews Earth & Environment, 2023, 4(2): 102-118.

Li, S., Li, X., Zhang, D. A fully coupled thermo-hydro-mechanical, three-dimensional model for hydraulic stimulation treatments. Journal of Natural Gas Science and Engineering, 2016, 34: 64-84.

Liu, B., Suzuki, A., Ito, T. Numerical analysis of different fracturing mechanisms between supercritical $CO_2$ and water-based fracturing fluids. International Journal of Rock Mechanics and Mining Sciences, 2020, 132: 104385.

Liu, Q., Deng, Y., Wang, T. One-dimensional nonlinear consolidation theory for soft ground considering secondary consolidation and the thermal effect. Computers and Geotechnics, 2018, 104: 22-28.

Lu, C., Han, W. S., Lee, S. et al. Effects of density and mutual solubility of a $CO_2$-brine system on $CO_2$ storage in geological formations: "Warm" vs. "cold" formations. Advances in Water Resources, 2009, 32(12): 1685-1702.

Lyu, X., Voskov, D. Advanced modeling of enhanced $CO_2$ dissolution trapping in saline aquifers. International Journal of Greenhouse Gas Control, 2023, 127: 103907.

Lyu, X., Wang, W., Voskov, D. et al. Multiscale modeling for multiphase flow and reactive mass transport in subsurface energy storage: A review. Advances in Geo-Energy Research, 2025, 15(3): 245-260.

MacMinn, C. W., Juanes, R. Buoyant currents arrested by convective dissolution. Geophysical Research Letters, 2013, 40(10): 2017-2022.

Mahmoodpour, S., Singh, M., Turan, A. et al. Simulations and global sensitivity analysis of the thermo-hydraulic-mechanical processes in a fractured geothermal reservoir. Energy, 2022, 247: 123511.

Martinez, M. J., Hesse, M. A. Two-phase convective $CO_2$ dissolution in saline aquifers. Water Resources Research, 2016, 52(1): 585-599.

Meng, Q., Jiang, X. Numerical analyses of the solubility trapping of $CO_2$ storage in geological formations. Applied Energy, 2014, 130: 581-591.

Moslehi, S., Fazeli, H., Doster, F. et al. Development of a reactive transport solver in MATLAB Reservoir Simulation Toolbox using the fully-implicit sequential iterative approach. Advances in Geo-Energy Research, 2025, 16(2): 114-130.

Nordbotten, J. M., Celia, M. A., Bachu, S. Injection and storage of $CO_2$ in deep saline aquifers: Analytical solution for $CO_2$ plume evolution during injection. Transport in Porous Media, 2005, 58(3): 339-360.

Otero, J., Dontcheva, L. A., Johnston, H. et al. High-Rayleigh-number convection in a fluid-saturated porous layer. Journal of Fluid Mechanics, 2004, 500: 263-281.

Pau, G. S. H., Bell, J. B., Pruess, K. et al. High-resolution simulation and characterization of density-driven flow in $CO_2$ storage in saline aquifers. Advances in Water Resources, 2010, 33(4): 443-455.

Pavan, T. N. V., Devarapu, S. R., Govindarajan, S. K. Numerical investigations on the performance of sc-$CO_2$ sequestration in heterogeneous deep saline aquifers under non-isothermal conditions. Gas Science and Engineering, 2024, 130: 205437.

Qu, H., Liu, J., Chen, Z. et al. Complex evolution of coal permeability during $CO_2$ injection under variable temperatures. International Journal of Greenhouse Gas Control, 2012, 9: 281-293.

Qu, Z., Zhang, W., Guo, T. Influence of different fracture morphology on heat mining performance of enhanced geothermal systems based on COMSOL. International Journal of Hydrogen Energy, 2017, 42(29): 18263-18278.

Reynolds, C. A., Blunt, M. J., Krevor, S. Multiphase flow characteristics of heterogeneous rocks from $CO_2$ storage reservoirs in the United Kingdom. Water Resources Research, 2018, 54(2): 729-745.

Safari, H., Balcom, B. J., Afrough, A. Characterization of pore and grain size distributions in porous geological samples - An image processing workflow. Computers & Geosciences, 2021, 156: 104895.

Sathaye, K. J., Hesse, M. A., Cassidy, M. et al. Constraints on the magnitude and rate of $CO_2$ dissolution at Bravo Dome natural gas field. Proceedings of the National Academy of Sciences of the United States of America, 2014, 111(43): 15332-15337.

Singh, M., Mahmoodpour, S., Singh, M. et al. Impact of thermo-hydro-mechanical process coupling for $CO_2$-water multiphase flow during geothermal energy extraction. Energy, 2025, 334: 137831.

Soboleva, E. B. Density-driven convection in an inhomogeneous geothermal reservoir. International Journal of Heat and Mass Transfer, 2018, 127: 784-798.

Sohal, M. A., Le Gallo, Y., Audigane, P. et al. Effect of geological heterogeneities on reservoir storage capacity and migration of $CO_2$ plume in a deep saline fractured carbonate aquifer. International Journal of Greenhouse Gas Control, 2021, 108: 103306.

van Genuchten, M. T. A closed-form equation for predicting the hydraulic conductivity of unsaturated soils. Soil Science Society of America Journal, 1980, 44(5): 892-898.

Vilarrasa, V., Olivella, S., Carrera, J. et al. Long term impacts of cold $CO_2$ injection on the caprock integrity. International Journal of Greenhouse Gas Control, 2014, 24: 1-13.

Wei, Z., Gao, K., Li, S. Integrated thermo-hydro-mechanical workflow for modeling $CO_2$ storage with fault activation risk. SPE Journal, 2025, 30(5): 2975-2995.

Wu, L., Hou, Z., Xie, Y. et al. Fracture initiation and propagation of supercritical carbon dioxide fracturing in calcite-rich shale: A coupled thermal-hydraulic-mechanical-chemical simulation. International Journal of Rock Mechanics and Mining Sciences, 2023, 167: 105389.

Xu, W., Chen, R., Hu, Y. et al. Effects of roughness on density-driven convection of dissolved $CO_2$ in discrete fracture-matrix system. Computers and Geotechnics, 2024, 166: 105996.

Zech, A., de Winter, M. A probabilistic formulation of the diffusion coefficient in porous media as function of porosity. Transport in Porous Media, 2023, 146(1): 475-492.

Zhang, Q., Xu, Q., Yang, Y. et al. Permeability heterogeneity effects on density-driven $CO_2$ natural convection and carbon sequestration efficiency. Fuel, 2024, 363: 130871.

Zhou, K., Wang, J., Xia, J. et al. Design and performance analysis of a supercritical $CO_2$ radial inflow turbine. Applied Thermal Engineering, 2020, 167: 114757.